A survey of Martian dust devil activity using Mars Global Surveyor Mars Orbiter Camera images

Jenny A. Fisher,[1] Mark I. Richardson,[1] Claire E. Newman,[1] Mark A. Szwast,[1] Chelsea Graf,[2] Shabari Basu,[1] Shawn P. Ewald,[1] Anthony D. Toigo,[3,4] and R. John Wilson[5]

Received 27 July 2003; revised 18 November 2004; accepted 22 December 2004; published 10 March 2005.

[1] A survey of dust devils using the Mars Global Surveyor (MGS) Mars Orbiter Camera (MOC) wide- and narrow-angle (WA and NA) images has been undertaken. The survey comprises two parts: (1) sampling of nine broad regions from September 1997 to July 2001 and (2) a focused seasonal monitoring of variability in the Amazonis region, an active dust devil site, from March 2001 to April 2004. For part 1, dust devils were identified in NA and WA images, and dust devil tracks were identified in NA images. Great spatial variability in dust devil occurrence is highlighted, with Amazonis Planitia being the most active region examined. Other active regions included Cimmerium, Sinai, and Solis. Numerous dust devil tracks, but very few dust devils, were observed in Casius. This may suggest dust devils here occur at local times other than that of the MGS orbit (~2 pm). Alternatively, variations in surface properties may affect the ability of dust devils to leave visible tracks. The seasonal campaign within Amazonis shows a relatively smooth variation of dust devil activity with season, peaking in mid northern summer and falling to zero in southern spring and summer. This pattern of activity correlates well with the boundary layer maximum depth and hence the vigor of convection. Global maps of boundary layer depth and surface temperature do not predict that Amazonis should be especially active, potentially suggesting a role for mesoscale circulations. Measurement of observed dust devils yields heights of up to 8 km and widths in excess of 0.5 km.

Citation: Fisher, J. A., M. I. Richardson, C. E. Newman, M. A. Szwast, C. Graf, S. Basu, S. P. Ewald, A. D. Toigo, and R. J. Wilson (2005), A survey of Martian dust devil activity using Mars Global Surveyor Mars Orbiter Camera images, *J. Geophys. Res.*, *110*, E03004, doi:10.1029/2003JE002165.

1. Introduction

[2] Suspended dust has a profound influence on the atmospheric circulation and thermal structure. Dust interacts with both solar and thermal infrared radiation, influencing atmospheric heating [*Zurek et al.*, 1992]. The Martian atmosphere is always dusty, although to what degree varies greatly with season [*Colburn et al.*, 1989; *Martin and Richardson*, 1993; *Toigo and Richardson*, 2000; *Liu et al.*, 2003; *Smith*, 2004]. Maximum dust opacities occur in southern spring and summer when large (regional or planet-encircling) dust storms can develop. By contrast, northern spring and summer is characterized by lower atmospheric dust abundances, without major storms and with little year-to-year variability.

[3] In many ways, the background dust haze is as important as the largest storms for determining the mean Martian climate: without the persistent background haze, models suggest that the global mean Martian atmosphere at midlevels (few tens of kilometers) would be as much as 10 K cooler than observed [*Basu et al.*, 2004]. Until recently, it had seemed plausible that this background haze might be maintained by global dust storms, with the opacity at any given time representing the slow fallout of small dust particles from the last big event. However, spacecraft global-mean observations show that northern spring and summer air temperatures and dust opacities repeat closely each year, regardless of whether there was a large storm during the prior southern spring or summer [*Liu et al.*, 2003]. Further, the dust fall-out following large storms is observed to be too rapid to be responsible for the bulk of northern spring/summer opacities [*Fenton et al.*, 1997; *Smith et al.*, 2002; *Liu et al.*, 2003]. Another possibility is that small storms during northern spring/summer produce the background haze. General Circulation Model (GCM) experiments have been conducted, however, using observed occurrences of small storms [*Cantor et al.*, 2001] to constrain the amount of dust injected [*Basu et al.*, 2004], and results suggest that a steadier, more continuous source

[1]Division of Geological and Planetary Sciences, California Institute of Technology, Pasadena, California, USA.
[2]La Canada High School, La Canada, California, USA.
[3]Department of Astronomy, Cornell University, Ithaca, New York, USA.
[4]Now at Department of Earth and Planetary Systems Science, Kobe University, Kobe, Japan.
[5]Geophysical Fluid Dynamics Laboratory, Princeton, New Jersey, USA.

0148-0227/05/2003JE002165$09.00

is needed. A plausible mechanism for this continuous dust lifting may be convective vortices, known as dust devils. Dust devils have been shown in laboratory experiments to be able to lift particles of various sizes, including extremely fine-grained particle sizes characteristic of Martian atmospheric dust, with lifting of such particles primarily due to the suction effect within (rather than to increased surface wind stresses around) the low-pressure vortex core [*Greeley et al.*, 2003]. Dust devils are well-known on the Earth, and they are a common form of daytime convection observed in terrestrial arid environments [*Renno et al.*, 1998]. In addition, dust devils and/or their tracks have been identified on Mars in Viking Orbiter images [*Thomas and Gierasch*, 1985; *Grant and Schultz*, 1987], Mars Pathfinder Lander imaging and meteorology station data [*Schofield et al.*, 1997; *Metzger et al.*, 1999; *Ferri et al.*, 2003], and Mars Global Surveyor (MGS) Mars Orbiter Camera (MOC) images [*Malin and Edgett*, 2001; *Cantor et al.*, 2002; *Balme et al.*, 2003].

[4] There is still debate about the significance of dust devils. *Balme et al.* [2003] studied dust devil tracks in the Hellas basin using MOC images. By comparing the estimated mass of dust lifted with the estimated global-mean fallout, they concluded that dust devils cannot raise enough dust. By contrast, *Ferri et al.* [2003] examined the abundance of dust devils observed by the Imager for Mars Pathfinder, and concluded that they can. GCM modeling of the Martian dust cycle, which matches the observed seasonal cycle of air temperatures by varying dust injection parameters within lifting parameterizations [*Basu et al.*, 2004], also suggests that dust devils not only can provide the haze but that this is the preferred solution.

[5] The aims of this study were to (1) collect statistics regarding the variation with time and location of Martian dust devils, using an initial multiregion analysis (sampling survey) to then focus on one region for the study of temporal variations; (2) test the prevailing thermodynamic theory of dust devils [*Renno et al.*, 1998] (which predicts dust devil activity on the basis of atmospheric data obtainable from either complementary observations or models); and (3) provide some estimates of the physical characteristics of dust devils observed from orbit.

[6] In the following sections, we initially describe the criteria used to select the regions used in the sampling survey, and the method used to identify dust devil activity in the MOC images. The results of the sampling survey are described next, which leads directly to the selection of the Amazonis region for more detailed study. The seasonal variation of activity in Amazonis is compared with contemporaneous Thermal Emission Spectrometer (TES) data. Measurements of the physical size are provided.

2. Study Approach, Definition of Study Regions, and Mapping Criteria

2.1. MOC Data Set and Data Processing

[7] Images from the MGS MOC are used as the basis for this survey of dust devil activity. MGS has been in orbit around Mars since October 1997, and in a mapping orbit since March 1999. The mapping orbit is a low polar, nearly sun-synchronous orbit, with nodal crossing times of roughly 2 am and 2 pm. Prior to mapping, the spacecraft was in an elliptical orbit, yielding variability of the local time of imaging observations (i.e., the local time at the surface location being imaged changed significantly during the course of aerobraking and was not 2 pm before the start of the mapping mission). The mission has been divided into phases, with AB, SP, and CAL (aerobraking, science phasing, and calibration) predating the mapping mission, and FHA, M, E and R (fixed high-gain antenna, mapping, extended and relay) covering the mapping, extended and relay mission. Data from the first aerobraking phase (AB1, beginning 15 September 1997) to the end of R15 (1 April 2004) have been included in this study.

[8] MOC is composed of three cameras, a narrow-angle (NA) monochromatic visible system (500-900 nm) with a maximum resolution of 1.4 m pixel^{-1}, and two wide-angle (WA) cameras with red and blue band passes [*Malin et al.*, 1992]. The WA red images (580–620 nm) have a maximum resolution of 230 m pixel^{-1}. Due to the fact that there are far fewer blue than red images (especially in the Amazonis study region) and that each blue image is almost always accompanied by a red image, blue images were not included in this survey.

2.2. Identification Criteria, Study Periods, and Regions

[9] Three different catalogs of dust devil-related activity were assembled as a part of the geographical sampling study. Two of these were direct observations of dust devils in NA and WA images (Figures 1a and 1b). These two imaging data sets provide somewhat different information about dust devil activity. The WA images provide much better spatial coverage than the NA images, while the NA images provide a much more complete survey of the dust devil size spectrum. A third derived data catalog provides a survey of dust devil tracks observed in the NA images (Figure 1c).

[10] Dust devils in WA images were identified as small, bright circular clouds with tapered elongated shadows. Dust devils in these images generally appear small, usually only a few pixels across (Figure 1a). Dust devils in NA images resemble those in WA images but on a larger scale. The actual devils usually appear as circular clouds, although on occasion the dust devil is not completely vertical, in which case the devil takes on an oblong, teardrop, or irregular shape when viewed by the nadir- (downward-) viewing NA camera. The shadows also often appear more complex in NA images, mirroring the shape of the devil (Figure 1b). Dust devil tracks appear as well-defined streaks on the Martian surface. Although generally much darker than the surrounding surface material, a few examples of light tracks have been identified. The tracks can be straight or curved and irregular, and often crisscross one another (Figure 1c). Occasionally a dust devil is seen creating the tracks, but the vast majority of images exhibiting tracks show no actual dust devils. Confusion with other (non dust devil related) surface features cannot be ruled out completely with individual images, but as will be seen in section 3.3, some significant confidence that the tracks we observed indeed result from dust devils is provided by the observed seasonal variation of these features (in a limited number of cases, overlapping images from different seasons show changes in these features, with some being erased and some being added over time).

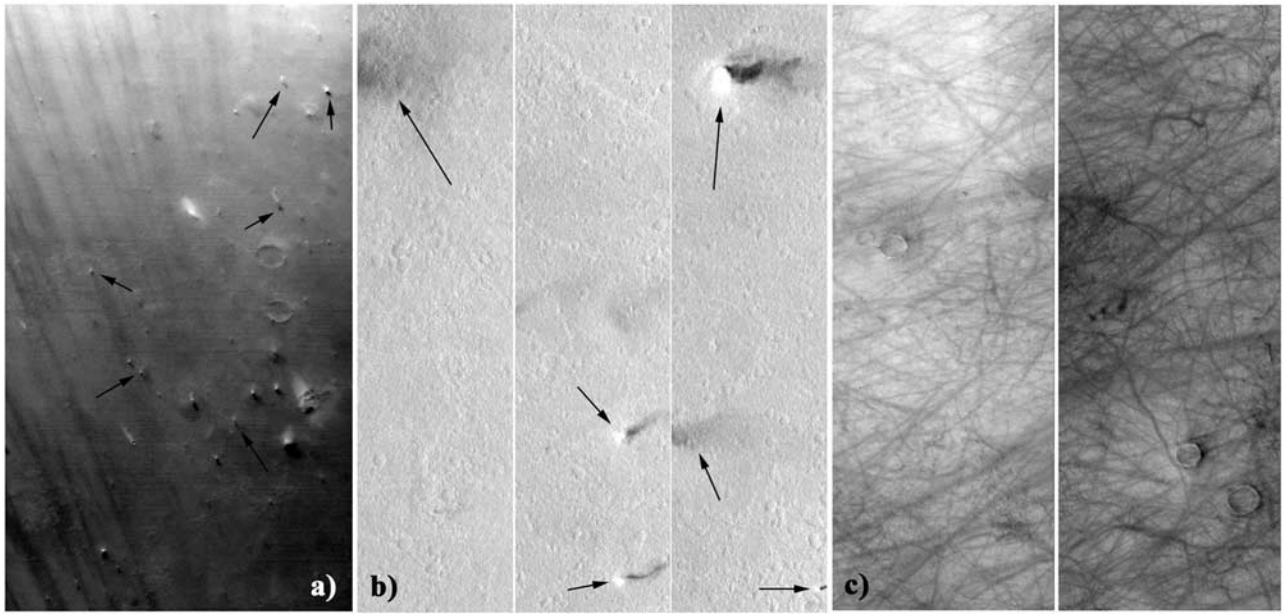

Figure 1. Examples of images from the regional surveys showing (a) dust devils in the MOC WA images (some examples indicated by arrows), (b) dust devils and shadows in MOC NA images (indicated by arrows), and (c) dust devil tracks observed in MOC NA images.

[11] The total number of available MOC images is huge (over 175,000 at the time of this study). In order to undertake a practical survey of dust devil activity, we have chosen to study selected regions on the surface, rather than images distributed over the entire planet. An alternative approach would have been to reduce the data volume by discarding some large fraction of the images (chosen randomly) before the survey, and then examine the global distribution of dust devils in the remaining images. As we shall demonstrate, however, the likelihood of dust devil detection is very low in most regions. It is sufficiently low that such an approach would result in very few dust devils being found.

[12] For the geographical sampling study, nine survey regions were selected on the basis of several different considerations (Figure 2). Amazonis Planitia (25–45°N, 145–165°W) and Casius (45–65° N, 255–285°W) were chosen on the basis of our initial, quick-look survey of MOC images. Hellas Planitia (15–60°S, 265–315°W) was selected due to its identification as a large atmospheric dust source and the site of initiation of many large-scale Martian dust storms [*Briggs et al.*, 1979]. Chryse Planitia (10–30°N, 30–60°W), the landing site of both the Viking 1 and Mars Pathfinder landers, was chosen on the basis of observations of dust devils at the site during the Mars Pathfinder mission [*Metzger et al.*, 1999], and Sinus Meridiani (10°S–10°N, 10°E–10°W) was selected as one of the two Mars Exploration Rover (MER) landing sites [*Squyres et al.*, 2003]. Utopia Planitia (25–45°N, 225–255°W) was selected on the basis of topographic similarity to Amazonis Planitia (similar latitude, relatively flat northern plains, near a major volcano). Solis Planum (15–45°S, 75–105°W) and Sinai Planum (10–20°S, 60–100°W) were chosen because of a historical association with dust storm onset regions [*Kahn et al.*, 1992]. Mare Cimmerium (10–45°S, 180–220°W) was selected on the basis of numerical atmospheric model predictions of high dust devil activity [*Newman et al.*, 2002]. For each region and category, statistics were compiled for four seasonal date bins centered on the equinoxes and solstices: $L_s = 45°–135°$ (northern summer solstice), $L_s = 135°–225°$ (northern autumn equinox), $L_s = 225°–315°$

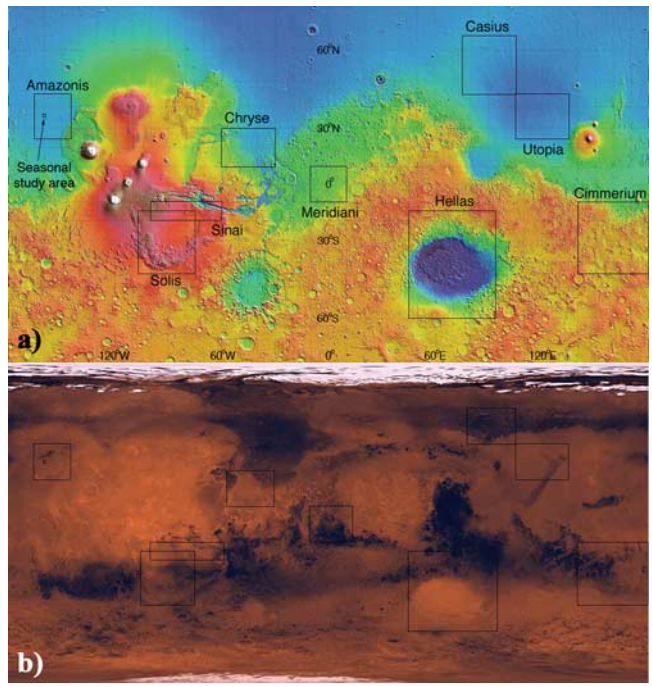

Figure 2. The nine geographic regions examined as a part of this study projected onto (a) Martian topography as derived by the Mars Orbiter Laser Altimeter (white/red regions show high terrain, grading to blue/purple low terrain) and (b) Martian albedo derived from the Viking cameras and Infrared Thermal Mapper. The study regions, including the Amazonis seasonal study region, are indicated with boxes.

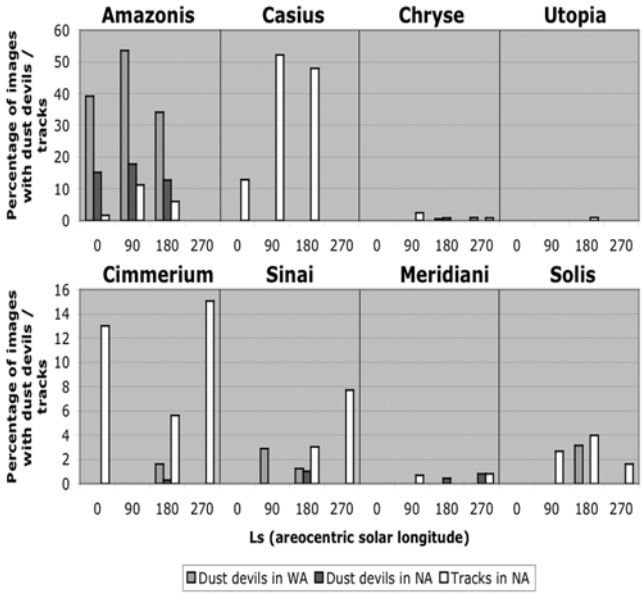

Figure 3. Histograms summarizing the data contained in Tables 1, 2, and 3. The percentage of images containing dust devils in WA and NA and those containing dust devil tracks are shown for each region except Hellas.

(northern winter solstice), and L_s = 315°–45° (northern spring equinox). The regional surveys were conducted for roughly one and a quarter Martian years (M01 to E06 or March 1999 to July 2001).

[13] For the seasonal monitoring study, the Amazonis region was selected to take advantage of the high abundance of dust devils (sections 3.1 and 3.2). After the first mapping year, observations were repeatedly targeted at a confined study site at roughly 36°N, 160°W (indicated in Figure 2). This study includes data from E02 to R15, covering northern summer in the second mapping year (March 2001) to northern spring equinox in the fourth (April 2004).

2.3. Thermal Emission Spectrometer Data

[14] Data from the MGS Thermal Emission Spectrometer (TES) is used to examine the seasonal variation of dust devil forcing for the Amazonis study site, and more generally in an attempt to understand why the Amazonis site exhibits a higher degree of dust devil activity at 2 pm than other sites on Mars. The data have been extracted from the PDS archive, selecting only nadir data. Only the highest quality data, as indicated by the various quality flags, have been used. For the calculation of the near-surface potential temperature gradient and the maximum planetary boundary layer depth, we use the archived retrieved temperature profiles [*Conrath et al.*, 2000]. The spectral surface temperature (derived from the TES spectrometer rather than the bolometer [*Christensen et al.*, 2001]) is used along with the official TES model (and archived) surface pressure.

3. Global Sampling Survey of Dust Devils and Their Tracks

[15] A total of 7910 MOC images (4320 WA and 3590 NA) were examined as a part of the global sampling survey. The seasonally binned results are presented in Tables 1, 2, and 3 (showing numbers of WA images found to contain dust devils, numbers of NA images containing dust devils, and numbers NA images exhibiting tracks, respectively) for each of the study regions. The number of images containing dust devils or dust devil tracks has been recorded in each regional and seasonal "bin", along with the total number of available images in each bin, and the resulting percentage frequency of dust devil activity. In this section, we describe the seasonal and spatial variability of dust devil activity. Two summary histograms, for the northern hemisphere and southern hemisphere regions except for Hellas, are shown in Figure 3.

3.1. Dust Devils in WA Images

[16] The WA image survey (Table 1) shows a large amount of spatial and seasonal variation in dust devil activity. Amazonis Planitia is by far the site of the most activity. Dust devils were identified in 140 of the 449 images of this region (about 32%; we will round to the nearest 2% in this part of the study to underscore the limited nature of the statistics). Furthermore, the region showed a

Table 1. Results of the Wide-Angle Survey[a]

Region	Season	Images With Dust Devils	Total Images	Percentage of Images With Dust Devils
Amazonis Planitia	315–45	29	74	39.19
	45–135	52	97	53.61
	135–225	59	173	34.10
	225–315	0	105	0
Casius	315–45	0	18	0
	45–135	0	35	0
	135–225	0	134	0
	225–315	0	45	0
Chryse Planitia	315–45	0	37	0
	45–135	0	99	0
	135–225	1	174	0.58
	225–315	1	111	0.90
Utopia Planitia	315–45	0	32	0
	45–135	0	67	0
	135–225	0	167	0
	225–315	0	99	0
Hellas Planitia	315–45	2	291	0.69
	45–135	0	226	0
	135–225	2	502	0.40
	225–315	0	330	0
Mare Cimmerium	315–45	0	111	0
	45–135	0	155	0
	135–225	4	249	1.61
	225–315	0	130	0
Sinai Planum	315–45	0	32	0
	45–135	2	69	2.90
	135–225	1	80	1.25
	225–315	0	32	0
Sinus Meridiani	315–45	0	58	0
	45–135	0	128	0
	135–225	0	179	0
	225–315	0	107	0
Solis Planum	315–45	0	59	0
	45–135	0	84	0
	135–225	5	160	3.13
	225–315	0	60	0

[a]Shown are the number of images containing dust devils, total number of images, and percentage of images containing dust devils for each season in each of the study regions.

Table 2. Results of the Narrow-Angle Survey[a]

Region	Season	Images With Dust Devils	Total Images	Percentage of Images With Dust Devils
Amazonis Planitia	315–45	9	59	15.25
	45–135	11	62	17.74
	135–225	17	133	12.78
	225–315	0	72	0
Casius	315–45	0	31	0
	45–135	0	46	0
	135–225	0	196	0
	225–315	0	96	0
Chryse Planitia	315–45	0	59	0
	45–135	0	119	0
	135–225	0	193	0
	225–315	1	115	0.87
Utopia Planitia	315–45	0	59	0
	45–135	0	90	0
	135–225	0	209	0
	225–315	0	119	0
Mare Cimmerium	315–45	0	123	0
	45–135	0	200	0
	135–225	1	320	0.31
	225–315	0	133	0
Sinai Planum	315–45	0	34	0
	45–135	0	83	0
	135–225	1	99	1.01
	225–315	0	39	0
Sinus Meridiani	315–45	0	71	0
	45–135	0	147	0
	135–225	1	224	0.45
	225–315	1	127	0.79
Solis Planum	315–45	0	68	0
	45–135	0	113	0
	135–225	0	175	0
	225–315	0	63	0

[a]Shown are the number of images containing dust devils, total number of images, and percentage of images containing dust devils for each season in each of the study regions.

strong preference for activity to occur in the local (northern) summer season (L_s = 45°–135°). About 54% of the images in this season contained dust devils, as compared to about 40% in northern spring (L_s = 315°–45°), ~34% in northern autumn (L_s = 135°–225°) and none in northern winter (L_s = 225°–315°). Individual images in this region showed from one to several tens of dust devils, often associated in large groups. The dust devils in the Amazonis region showed a large range of sizes, with some devils up to several kilometers in height (see section 5).

[17] No other region surveyed showed nearly the amount of dust devil activity observed in Amazonis Planitia. However, some limited numbers of dust devils (appearing in >1.5% of images in at least one season) were observed in WA images of Mare Cimmerium, Sinai Planum and Solis Planum. In Sinai Planum, dust devils were most active in northern summer when ~3% were observed (the highest percentage outside Amazonis). In Mare Cimmerium and Solis Planum they were most common in northern autumn (local spring). No dust devils were observed in the WA survey for Sinus Meridiani, corresponding to the Opportunity rover landing site, or Utopia.

3.2. Dust Devils in NA Images

[18] Dust devils were found even less frequently in NA images (Table 2) than in WA images, due to the reduced area covered (hence the smaller probability of detection, unless a particularly active region of typical NA size were to have been targeted). Throughout the entire regional survey, dust devils were identified in only 42 NA images. Of these, 37 were located in the Amazonis Planitia region. In all other regions, no more than two images were found to contain dust devils, and no dust devils were observed at all in NA images of Solis, Casius, or Utopia.

[19] A slight seasonal preference for dust devil activity to occur during northern summer was again observed in Amazonis, with about 18% of images containing dust devils (versus 16% in spring, 12% in autumn). Again, no dust devils were observed in Amazonis during northern winter (southern summer). In the other survey regions the numbers observed (in <2% of images for all regions and seasons) were too low to make strong conclusions.

3.3. Dust Devil Tracks

[20] Eight of the study regions were examined for evidence of dust devil tracks (Hellas has been the focus of a dedicated study by *Balme et al.* [2003], which is not reproduced here). The results of our survey are contained in Table 3.

[21] Dust devil tracks provide complementary information to that obtained from direct detection of dust devils. While the latter provides an instantaneous sampling, the former provides a record of dust devils from all local times

Table 3. Results of the Narrow-Angle Dust Devil Track Survey[a]

Region	Season	Images With Tracks	Total Images	Percentage of Images With Tracks
Amazonis Planitia	315–45	1	59	1.69
	45–135	7	62	11.29
	135–225	8	133	6.02
	225–315	0	72	0
Casius	315–45	4	31	12.90
	45–135	24	46	52.17
	135–225	94	196	47.96
	225–315	0	96	0
Chryse Planitia	315–45	0	59	0
	45–135	3	119	2.52
	135–225	0	193	0
	225–315	1	115	0.87
Utopia Planitia	315–45	0	59	0
	45–135	0	90	0
	135–225	2	209	0.96
	225–315	0	119	0
Mare Cimmerium	315–45	16	123	13.01
	45–135	0	200	0
	135–225	18	320	5.63
	225–315	20	133	15.04
Sinai Planum	315–45	0	34	0
	45–135	0	83	0
	135–225	3	99	3.03
	225–315	3	39	7.69
Sinus Meridiani	315–45	0	71	0
	45–135	1	147	0.68
	135–225	0	224	0
	225–315	1	127	0.79
Solis Planum	315–45	0	68	0
	45–135	3	113	2.65
	135–225	7	175	4.00
	225–315	1	63	1.59

[a]Shown are the number of images containing dust devil tracks, total number of images, and percentage of images containing dust devil tracks for each season in each of the study regions.

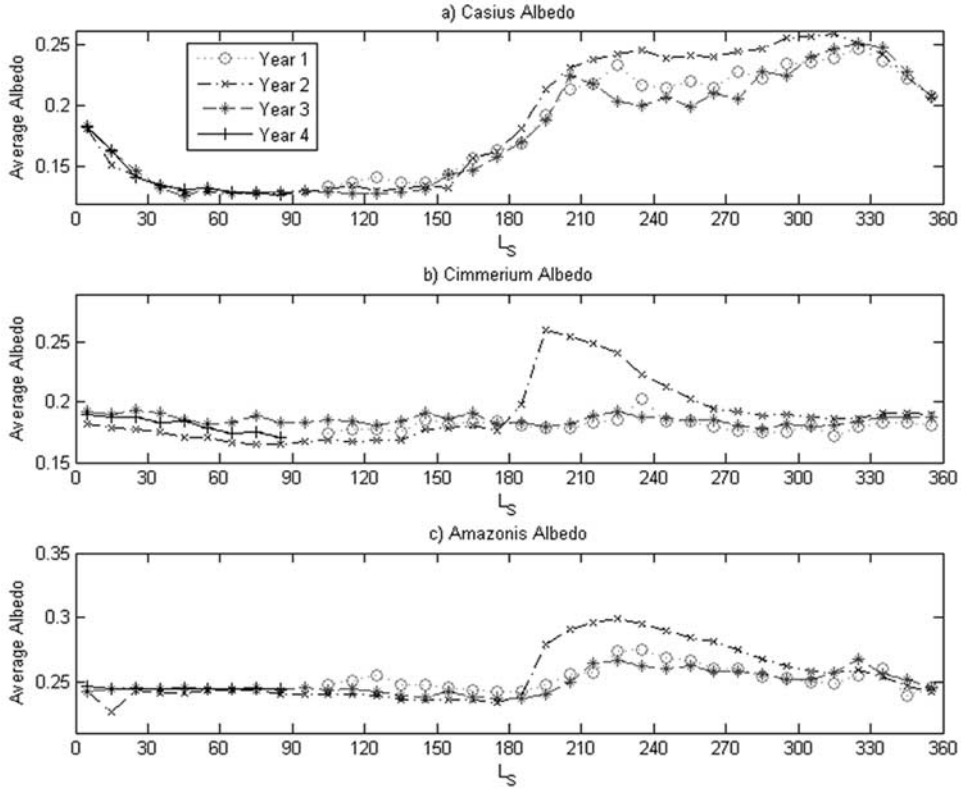

Figure 4. The seasonal cycles of albedo measured by the TES visible bolometers for the study sites at (a) Casius, (b) Cimmerium, and (c) Amazonis. The large seasonal variation at Casius is due to the formation of seasonal ice clouds and ice cap in parts of the region between L_s = 150° and 30°. The much smaller range for Cimmerium and Amazonis is due to the seasonal cycle of atmospheric dust opacity. The large deviations in the second MGS mapping year ("Year 2") are associated with the 2001 global dust storm [*Smith et al.*, 2002; *Strausberg et al.*, 2005].

and integrated over some extended period. This period is determined by the rate of dust settling, which can eradicate tracks. However, dust devil tracks can only be observed in locations in which tracks are apt to form. This requires both that dust devils occur and that the removal of a small amount of dust (few to few tens of microns thickness) exposes a surface of sufficiently different albedo to be observable.

[22] One concern might be that the dust devil tracks accumulate over a very long timescale (much greater than one year), such that seasonal observations are of little value. However, Table 3 shows that in all of the study regions, zero dust devil tracks are observed for at least one seasonal bin. In addition, *Balme et al.* [2003] found similar erasure of dust devil tracks for Argyre and Hellas. These results suggest that the dust devil tracks do not continuously accumulate and are reset at some point during the annual cycle.

[23] The vast majority of dust devil tracks in this study were observed in Casius. In northern summer and autumn (L_s = 45°–225°), they appeared in roughly 50% of the images (note that individual tracks were not counted). This abundance of tracks is in striking contrast with the results of WA and NA dust devil surveys for Casius, which exhibited no dust devils in 601 images. This could be explained in one or more of the following ways:

[24] 1. Dust devils at Casius do not occur at 2 pm local time (though this should be a time of high occurrence [*Murphy and Nelli*, 2002; *Toigo et al.*, 2003]),

[25] 2. Dust devils at Casius are too small to be observed (but this is not consistent with their absence in 387 NA images) or do not contain enough dust to be evident,

[26] 3. Casius may only contain a thin surface veneer of dust over a darker surface, allowing even small dust devil tracks to be seen,

[27] 4. Net dust deposition rates at Casius may be particularly low, allowing tracks to remain for a long time once formed.

[28] Options 3 and 4 are coupled in that a region of low net deposition is likely to have only a thin veneer of dust. Option 2 seems least likely as the survey for dust devils has a range of resolutions, and the fact that dust devil tracks form readily implies that there is sufficient dust to allow convective vortices to be made visible by the presence of dust. Option 1 cannot be ruled out, as local meteorology may be important for suppressing dust devil activity at what should otherwise be an active period of the day. Options 3 and 4 are supported by the relatively low albedo of the Casius region (~0.13) as measured by TES (Figure 4a), and by the fact that the albedo remains at essentially this value from midspring to midsummer (L_s = 40°–140°). In northern

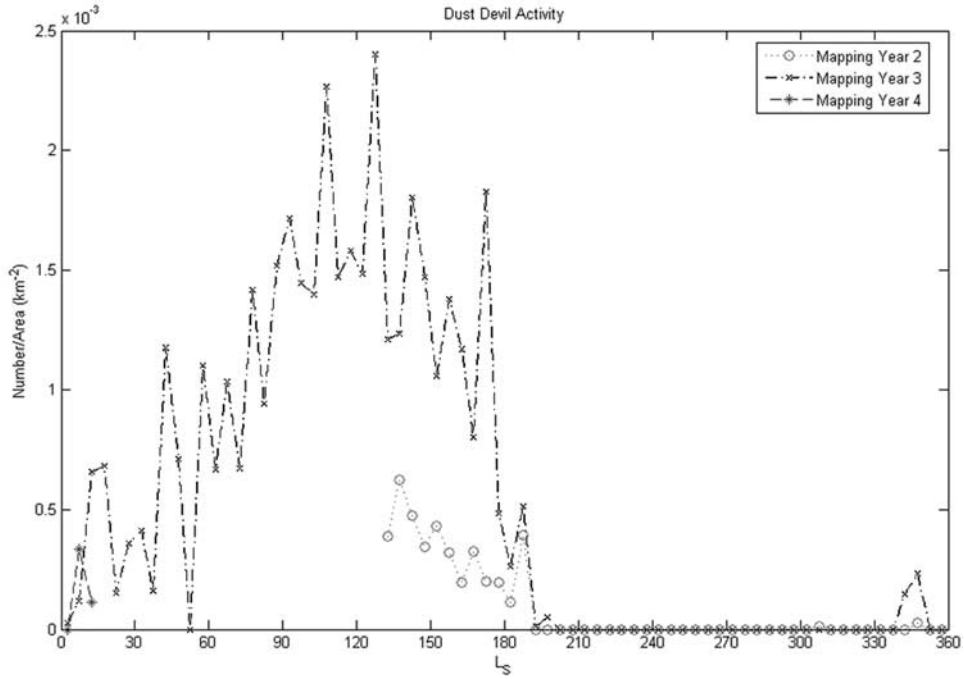

Figure 5. The number of dust devils per unit area counted in the Amazonis seasonal study region as a function of seasonal date (L_s) for the second, third, and fourth MGS mapping years. All data were collected from MOC WA images, as described in the text. There was insufficient coverage in the first mapping year.

autumn and winter, the large increase in albedo is due to encroachment by the seasonal ice cap, rather than deposition of large amounts of dust. This covering may also contribute to the lack of tracks in these seasons.

[29] Mare Cimmerium has the next highest number of images with dust devil tracks (54), but this survey also contains the highest number of total images (776), such that the fraction of images with tracks never exceeds 16%. Cimmerium is in the southern hemisphere, such that the observed lack of tracks during the $L_s = 45°–135°$ bin is consistent with Casius in the absence of evidence for dust devil activity in local winter. Further, Cimmerium is sufficiently far equatorward that the seasonal ice cap is not an issue. Indeed, the trend of activity, with the summer solsticial bin showing the highest track abundance, followed closely by the autumnal equinox, with much fewer tracks in the vernal equinox bin is very similar to Casius. For Cimmerium, a higher percentage of images contained tracks than dust devils, possibly for similar reasons to those described for Casius. The albedo of the Cimmerium region (Figure 4b) is higher than Casius ($\sim$0.17–0.19), suggesting somewhat higher surface dust coverage. The seasonal variation of albedo is sufficiently flat that no seasonal cycle of dust lifting and deposition can be seen; the albedo shown in Figure 4b is the total albedo including the effects of aerosols, such that the variation that is evident in this figure is associated with atmospheric dust opacity. This is especially prominent in Year 2, for the 2001 global dust storm peaking at about $L_s = 195°$.

[30] Amazonis has a similar seasonal trend (of track observation) to Casius and Cimmerium, but has many more direct images of dust devils than of dust devil tracks. However, it has the next highest abundance of images with tracks (16 out of 326) in this survey. The albedo of Amazonis, at $\sim$0.24–0.25 (Figure 4c), may explain this: ample dust makes dust devils easily visible, while the surface is sufficiently dust coasted that a darker, underlying surface cannot easily be exposed to yield a visible dust devil track. The remaining regions have very low dust devil track occurrence, and thus seasonal trends are hard to distinguish.

[31] Two significant conclusions can be taken away from the dust devil track survey. First, neither the survey of 2 pm dust devils nor that of their tracks gives a complete picture of dust devil activity in isolation. Second, in regions where sufficient tracks can be observed, the seasonal trend of tracks is both significant (track lifetimes appear to be subannual) and matches that of the dust devils themselves.

3.4. Summary of Results of the Global Survey

[32] Overall, both direct and track observations show a preference for dust devil activity to peak during local summer. For each region shown in Figure 3, this corresponds to the second bin in the upper (northern hemisphere) portion of the chart, and to the fourth bin in the lower (southern hemisphere) portion of the chart. Of the regions selected, Amazonis appears to be the most active (at least in terms of dust devils produced at 2 pm, which is likely to be within a few hours of their peak occurrence time [*Murphy and Nelli*, 2002; *Toigo et al.*, 2003; *Ferri et al.*, 2003]). Casius has the largest number of images with dust devil tracks, but very few dust devils were directly observed here. Previous GCM studies [*Newman et al.*, 2002; *Basu et al.*, 2004] have shown Amazonis to be a region of moderate to high dust lifting, but predict little dust devil activity as far

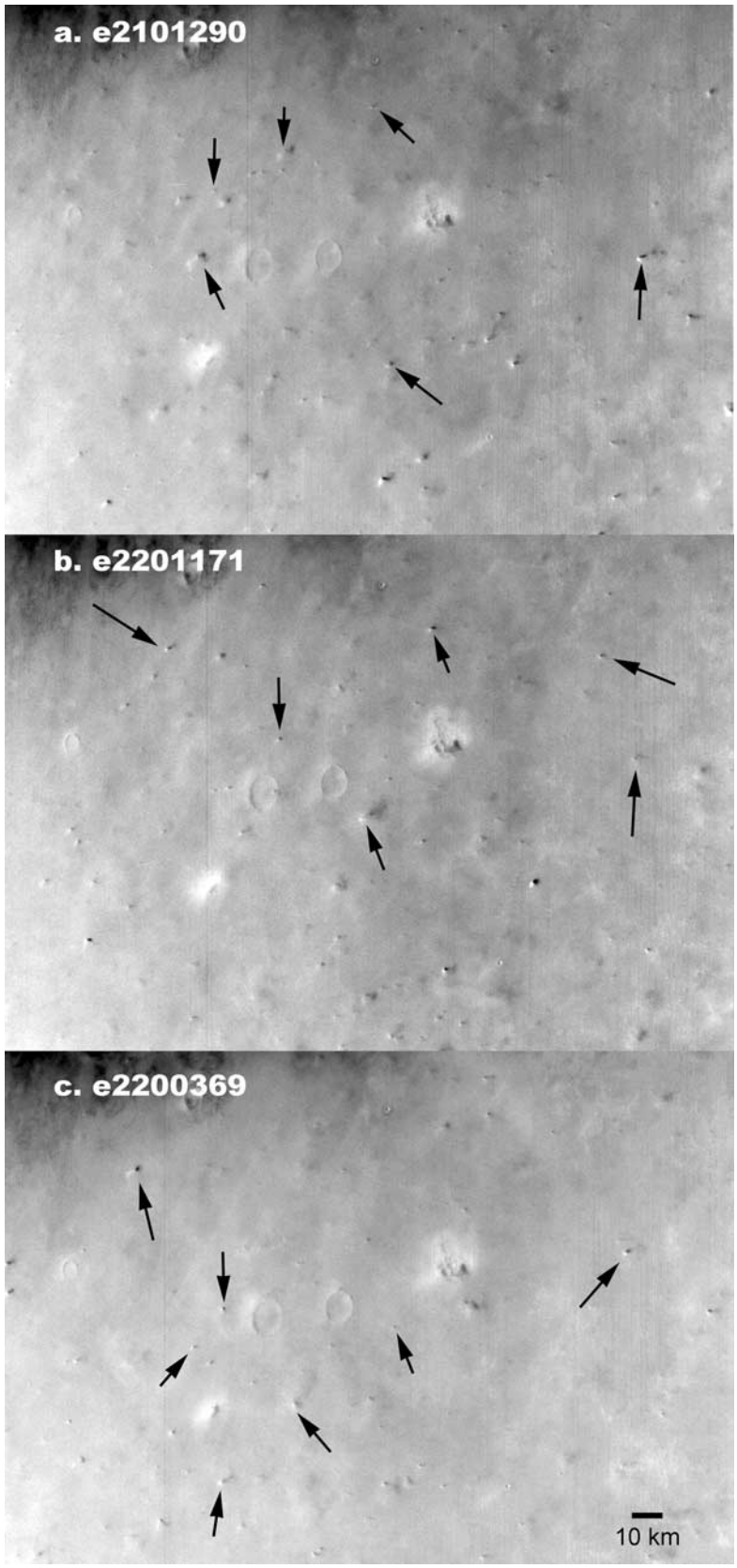

Figure 6. Example MOC WA frames from the Amazonis seasonal study region. The images were collected between L_s = 85° and L_s = 92° in the third mapping year. The images are centered on roughly 36°N, 160°W, with scale as indicated. North is up on all frames, with roughly the same area covered in each frame. Examples of dust devils are indicated with arrows (note that not all dust devils in frame are thus indicated).

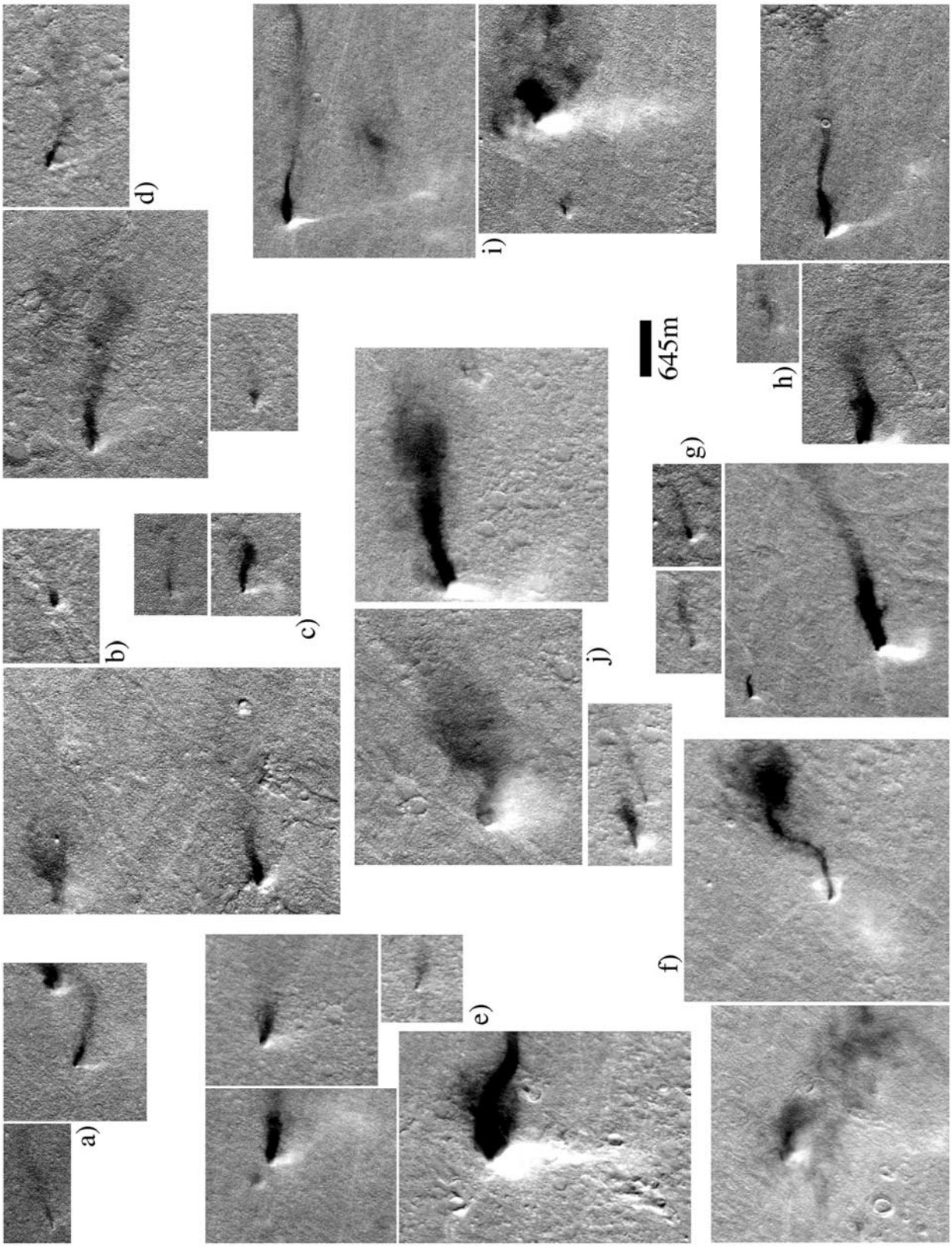

Figure 7

north as Casius. Future work will involve comparing GCM predictions with dust devil observations.

4. Dust Devil Seasonal Survey in Amazonis

[33] The data provided in Tables 1 and 2 suggest that Amazonis exhibits an unusually large number of dust devils of sufficient size to be observed by the MOC WA camera at the roughly 2 pm local time of the MGS orbit. Beginning in March 2001 (E02), during Martian northern summer (L_s = 130°), MOC WA images were collected over a study region centered at roughly 36°N, 160°W and spanning a few degrees in each direction. (Note that this is not the same study region area defined for Amazonis as part of the regional study; for this detailed seasonal study, the area is much smaller, as shown in Figure 2). The scaled pixel widths of the MOC WA images used in this study varied but were typically between 250 and 300 m. For this paper, images collected between March 2001 (E02) and March 2004 (R15) have been examined. This collection of 202 good quality WA images spans almost one and three quarter Martian years, from L_s = 130° in mapping year 2, to L_s = 12° in mapping year 4.

[34] The numbers of dust devils within each image were counted for this survey, and then the activity (defined as the number of dust devils per unit area) calculated from this number and the projected image area. The dust devils were counted three times, once each by three of the authors (CG, JAF, and MIR). The results are shown in Figure 5. The figure provides a very much more detailed picture of the behavior of dust devils in Amazonis, but one which squares well with the regional survey (section 3.1): dust devil activity is significant in northern spring and summer, trailing to nothing in autumn and winter. During the late northern summer of the second mapping year, the activity is as much as a factor of 3 to 4 lower than at the same season in the third mapping year. However, we do not believe this to represent real interannual variability. Instead, the images in the third mapping year benefited from much better exposures, producing much crisper images. As such, we believe the third mapping year to provide a better representation of the true dust devil activity in northern summer than the second year data. Individual images at the peak of this activity had as many as 83 dust devils, and typical images from this peak activity period in Year 3 are shown in Figure 6. This figure highlights example dust devils of various sizes. For an individual image the decision as to whether small features are actually dust devils might be problematic, but in this study the availability of frequent images of the same location allowed identification of dust devils on the basis of features which were absent from earlier and later images. In other words, any "now you see it, now you don't" feature, of the right shape (line or point), and exhibiting a shadow on the correct side, was considered a dust devil. In a limited number of cases, NA images were collected along with the WA survey images. These images allowed the dust devils to be observed in greater detail. Some idea of the nature and variation of the shape and size of the dust devils can be gained from examination of Figure 7. Only the largest of these dust devils are caught in the WA survey.

4.1. Dust Injection Capacity at Amazonis

[35] The peak dust devil activity for the Amazonis seasonal study region is in mid northern summer (L_s = 120°–130°), with roughly 2.5 dust devils per 10^3 km^2. By definition, this is the activity of dust devils large enough to be resolved in the MOC WA images. Assuming that the smallest resolvable dust devil is 2 pixels by 2 pixels (or roughly 0.25 km^2 in horizontal cross sectional area) and that this is characteristic of the WA dust devils, the fractional area covered by dust devils peaks at about 6×10^{-4} (if the area is instead 0.06 km^2 corresponding to 1 pixel by 1 pixel, the fractional area is closer to 1.5×10^{-4}). These areal fraction numbers can be compared to those calculated from Imager for Mars Pathfinder (IMP) data by *Ferri et al.* [2003], who found a value of 2×10^{-4}. The IMP study included a broader spectrum of dust devil sizes (extending to vortices as small as 11 m), such that the peak Amazonis areal fraction likely represents an activity between a factor of a few and an order of magnitude higher than observed by IMP. This is consistent with the relative activity found for Amazonis and Chryse in the regional study (section 3.1). Using an individual dust devil lifting capacity of roughly 10^{-4} kgm^{-2} s^{-1} [*Ferri et al.*, 2003] (the area in this case referring to the cross sectional area of the dust devil), the Amazonis dust devils at their peak may be lifting about 2000 kg of dust per second, integrated over the 36,000 km^2 (or about 6×10^{-8} kgm^{-2} s^{-1}, where the area is now the total surface area of the region) this would correspond to an increase in opacity of about 2×10^{-5} s^{-1}, if not balanced by deposition. Deposition is of course critical. The rates of injection estimated for Amazonis are sufficiently high that they would overwhelm observed deposition rates at the Pathfinder site [*Ferri et al.*, 2003], although Amazonis may see higher deposition as well as injection rates, relative to the Pathfinder site. In either case, the Amazonis observations are consistent with dust devils playing an important and potentially dominant role in the maintenance of the background dust haze on Mars.

4.2. Observed Local Time Variation of Dust Devil Development

[36] The abundance of dust devils at Amazonis made this location an attractive target for observations by the Mars Odyssey Thermal Emission Imaging System (THEMIS). The THEMIS visible camera, yielding images with pixel sizes of between 20m and 100m, collected a small number of samples of the seasonal study region during the northern spring and summer of MGS mapping year 3. The 17 visible images in this collection are listed in Table 4. The THEMIS images were collected at local times varying between from

Figure 7. Collection of dust devils captured within the Amazonis seasonal study region in NA images taken concurrently with the WA survey frames. Segments of each image containing dust devils are grouped together in the figure. All segments are shown at the same scale (indicated). Segments are taken from MOC NA images (a) e2000851, (b) e2001304, (c) e2101170, (d) e2200666, (e) e2300955, (f) e2301274, (g) r0100879, (h) r0200052, (i) r0200468, and (j) r0200854.

Table 4. THEMIS Visible Images Collected for the Amazonis Seasonal Study Area During Northern Spring and Summer of the Third MGS Mapping Year[a]

THEMIS Image	Seasonal Date (L_s)	Local Time
V02240007	28.4°	3:55 pm
V02502006	38.18°	4:05 pm
V03613003	78.5°	4:36 pm
V04075011	95°	4:48 pm
V04125006	97°	4:48 pm
V04824043	123.3°	5:03 pm
V04849019	124.3°	5:03 pm
V04874006	125.3°	5:03 pm
V05211009	138.7°	5:11 pm
V05261019	140.7°	5:12 pm
V05286015	141.8°	5:13 pm
V05473038	149.5°	5:17 pm
V05498015	150.6°	5:17 pm
V05523007	151.7°	5:18 pm
V05548017	152.7°	5:19 pm
V05598019	154.8°	5:20 pm
V06035005	174.2°	5:25 pm

[a]No unambiguous dust devils were observed in any of the images.

just before 4 pm to 5:25 pm, allowing activity at local times 2–3 hours later than the MOC imagery to be examined. In none of the images were unambiguous dust devils observed. While the abundance of THEMIS images in this region is relatively low, the results of the MOC NA survey (section 3.1) suggest that at least 2 of the 17 THEMIS frames ought to have contained unambiguous dust devils, if the fraction of images containing dust devils were the same. With the greater area of THEMIS frames (typically ~560 km^2 compared to at most 200 km^2 for MOC NA), the increase in fraction of images containing dust devils between MOC NA and WA suggests even more THEMIS images should have captured dust devils. We interpret the fact that they did not to indicate that dust devil activity diminished significantly between 2 pm and 5 pm at the Amazonis seasonal study site. Increased coverage of this site by THEMIS, the Mars Express High Resolution Stereo Camera, and other orbiter imaging systems in coming years would greatly help constrain the local time behavior of dust devils and help further constrain theory.

4.3. Thermal Forcing of Dust Devils

[37] Dust devils are a form of boundary layer convection: motions driven in response to strong solar heating of the surface, and yielding a net heat transfer from the surface to the atmosphere. Conceptually, the strength of dust devil activity ought to scale with factors diagnostic of boundary layer convective activity. Specifically, the thermodynamic theory of dust devils developed by *Renno et al.* [1998], and used to predict net dust devil injection in global numerical models [*Newman et al.*, 2002; *Basu et al.*, 2004], relates dust devil activity (*DDA*) to the depth of the well-mixed boundary layer and the sensible heat flux at the surface:

$$DDA = \eta \times H, \tag{1}$$

$$\eta = 1 - b, \tag{2}$$

$$b = \frac{p_s^{\kappa+1} - p_{top}^{\kappa+1}}{(p_s - p_{top}) \times (\kappa + 1) \times p_s^{\kappa}}, \tag{3}$$

$$\kappa = \frac{R}{c_p}, \tag{4}$$

where H is the surface sensible heat flux, p_s is the surface pressure, p_{top} is the pressure at the top of the boundary layer, R is the gas constant, and c_p is the gas specific heat capacity.

[38] Some estimate of the drive for *DDA* as a function of season for the Amazonis seasonal study region can be determined from the MGS TES data. While the sensible heat flux at the surface cannot be determined directly from data, some sense of the seasonal variation can be obtained from the surface temperatures, and the lower atmosphere potential temperature gradient. The thermodynamic efficiency, η, can be directly estimated from the TES data, insofar as the PBL top can be defined in terms of the potential temperature structure in the lower atmosphere (see below). Thus while theory cannot be uniquely validated, consistency can be checked.

[39] Key thermodynamic variables derived from the TES data are shown in Figure 8. The surface temperature trend appears as a skewed sine wave, with maximum temperatures in northern summer and minimum in winter. The location of the Amazonis study region at roughly 36°N means that maximum zenith angle of the sun at noon occurs at northern summer solstice. However, because of the eccentricity of the orbit, the peak insolation and peak surface temperatures do not occur until later in northern summer (note that this is not the same kind of phase delay of temperatures experienced on Earth, where peak temperatures are delayed past the June solstice into July and August by the thermal inertia of the oceans). The resulting relatively steady, high surface temperatures during northern spring and summer, followed by an increasingly sharp drop in temperatures after L_s = 150° and low temperatures through northern autumn and winter (southern spring and summer) is in good qualitative agreement with the dust devil activity (Figure 5). To the extent that sensible heat goes as the surface temperature and the near-surface potential temperature gradient, peak fluxes would be expected between L_s = 120° and 150°. The decreasing trend in surface pressure at this time would tend to push the maximum toward L_s = 120° for a fixed vigor of convective mixing. While we cannot measure the vigor of convective mixing, we can quantify the degree of instability of the lower atmosphere (between the surface and the 4.75 mbar level, for example, as used here). The potential temperature gradient would be zero for a neutrally stable atmosphere, and increasingly negative for increasing instability. Figure 8f shows that the greatest instability occurs in mid northern summer at Amazonis, suggesting the greatest drive for convective mixing vigor occurs at this season.

[40] The thermodynamic efficiency in equation (1) can be written in terms of the planetary boundary layer (PBL) height, or, more accurately, the pressure drop between the surface and the boundary layer top. The maximum height of the mixed boundary layer, in turn, can be estimated by finding the level at which the atmospheric potential temperature first exceeds the potential temperature of an air parcel at the surface and with a temperature equal to that of the surface. This level corresponds to the first level of the atmosphere at which the air has greater buoyancy (lower density when brought to the same pressure adiabatically)

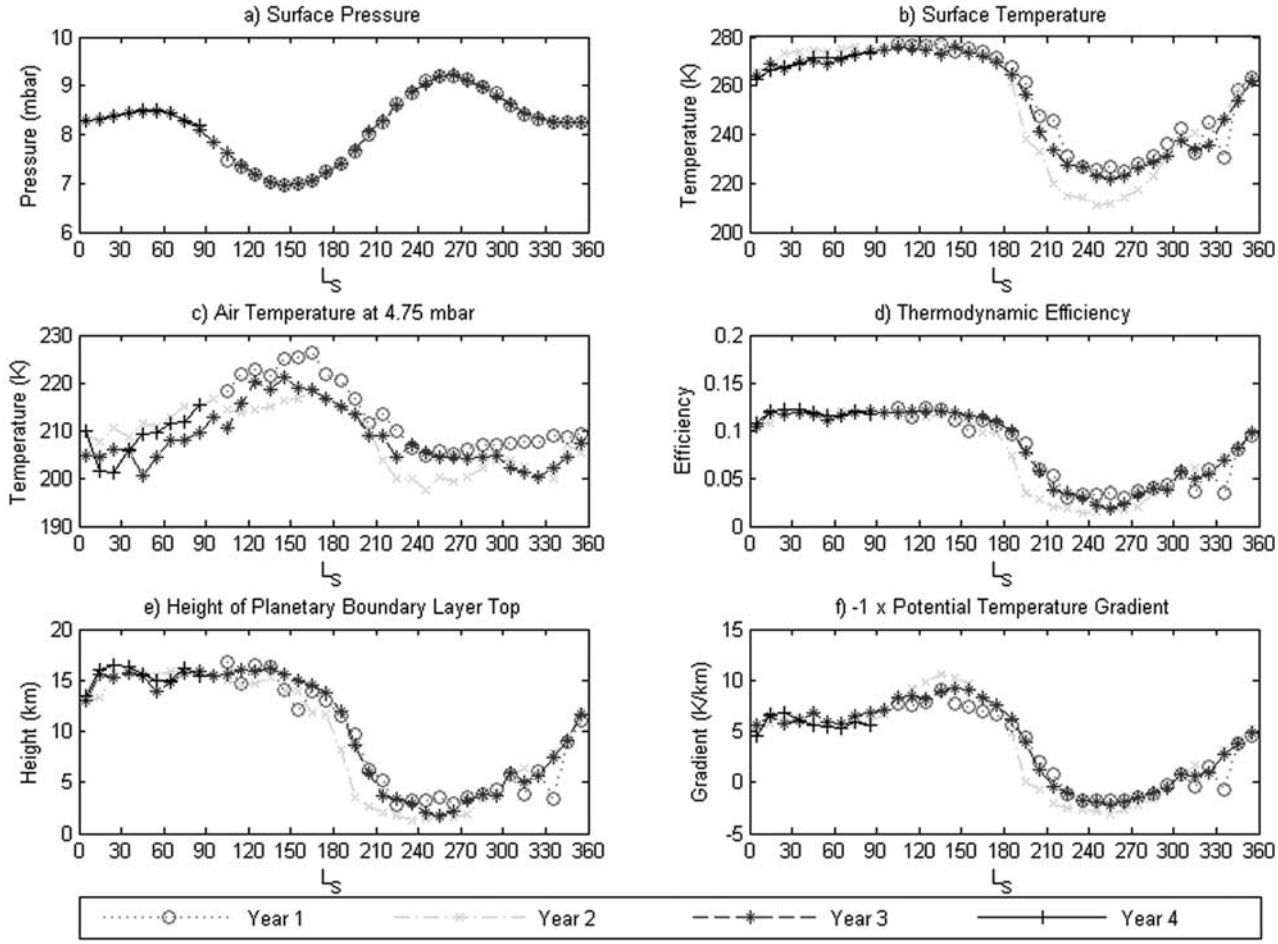

Figure 8. Thermal Emission Spectrometer (TES) data, estimate surface pressures, and derived quantities for the Amazonis seasonal study region. Data were binned for 34°N–37°N and 155°W–161°W. The (a) estimated surface pressure, (b) surface temperature, and retrieved temperature profile (values at 4.75 mbar shown in Figure 8c) were used to calculate (d) the thermodynamic efficiency of the planetary boundary layer (PBL) convective heat engine (see text and *Renno et al.* [1998]), (e) the maximum PBL top height, and (f) the lower atmosphere potential temperature gradient. The maximum PBL top height is estimated by finding the atmospheric level at which the potential temperature equals that of an air parcel on the surface and at the surface temperature; it is therefore likely an overestimate, being about twice the generally accepted value.

than the equilibrated surface air parcel: it defines the maximum reach of thermal convection driven from the surface. It is likely an overestimate of the true mixed PBL height since the air even very close to the surface can be considerably cooler than the surface (this was likely true at the Mars Pathfinder landing site, although surface temperatures were not measured, a strongly super-adiabatic near-surface temperature profile was [*Schofield et al.*, 1997]). The values of the maximum PBL height calculated from the TES data (Figure 8e) are about a factor of 2–3 larger than theoretical and model estimates [*Gierasch and Goody*, 1967; *Haberle et al.*, 1993; *Toigo et al.*, 2003; *Basu et al.*, 2004]. This corresponds to an overestimate of the thermodynamic efficiency of a little less than a factor of 2–3 (compare our Figure 8 with Figure 3 from *Newman et al.* [2002] and Figure 2 from *Basu et al.* [2004]).

[41] Comparison of Figures 5 and 8 suggests that activation of dust devils requires a critical value of the convolved sensible heat flux and thermodynamic efficiency to be exceeded. During northern autumn and winter, the boundary layer depth and hence the thermodynamic efficiency are low. This is mirrored by the lower atmosphere (~4 km) potential temperature gradient, indicating the vigor of mixing, and all of these follow to first approximation the trend in surface temperature. From Figure 8, it would appear that near-surface (~0–4 km) potential temperature gradients greater than 5 K/km and PBL development to deeper than about 10 km (corresponding to a thermodynamic efficiency of about 0.1) is necessary to trigger dust devils. However, our estimated over-prediction of PBL depth of 2–3 should be noted when using these numbers.

[42] Beyond the binary "on-off" nature of activity between northern spring/summer and northern autumn/winter, the details of the dust devil activity trend are a little harder to explain. The rise and fall of activity is smooth (the switch "on" and "off" is not sharp), but with a more rapid fall than rise, and the activity peaks at around $L_s = 120°$ (Figure 5). PBL depth and thermodynamic efficiency are actually rather

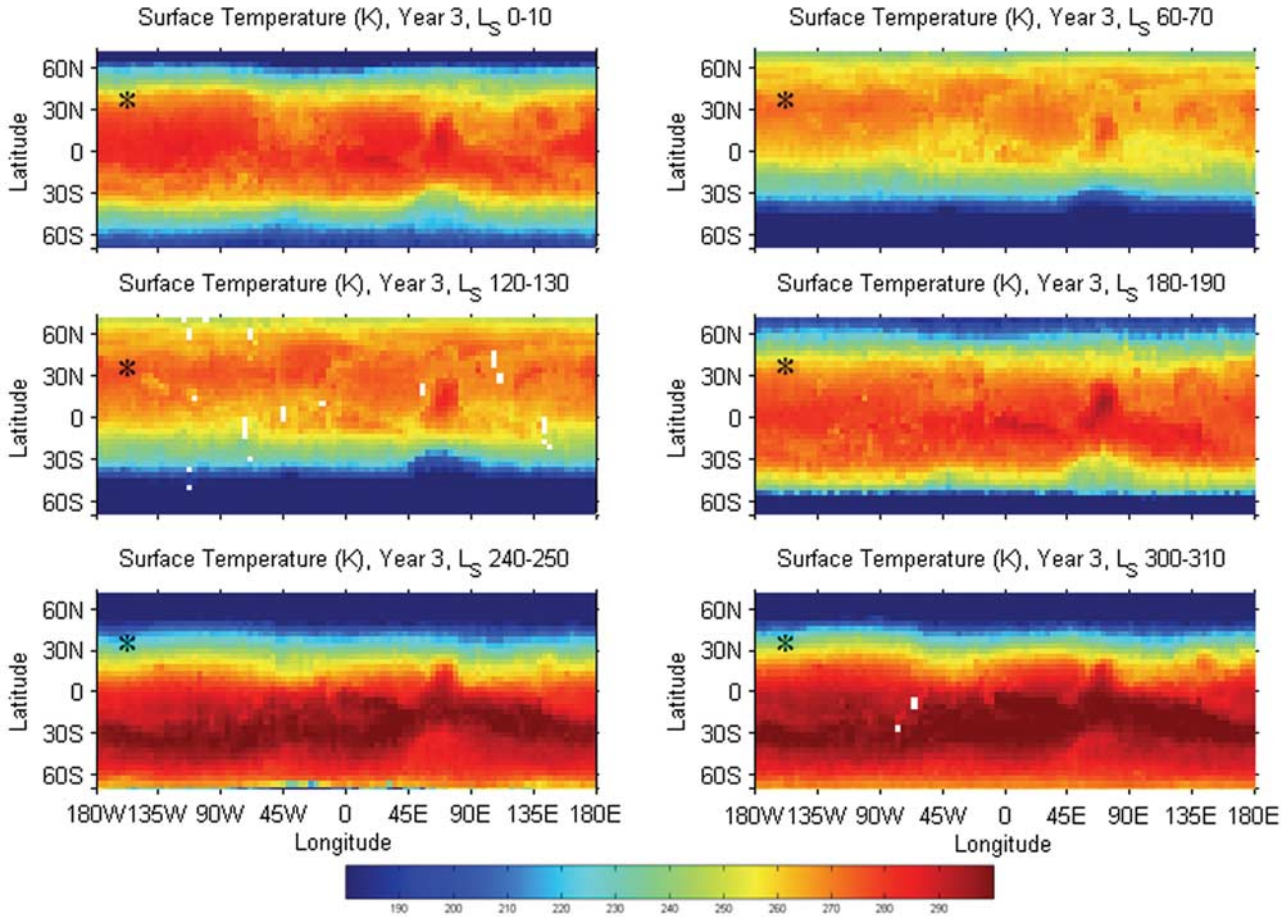

Figure 9. The geographical and seasonal distribution of 2 pm ground temperatures estimated from TES data for six 10° of L_s bins, as indicated. An asterisk marks the location of the Amazonis seasonal study region. Color bar runs from 180 to 300 K.

flat throughout northern spring and summer, and would predict a similarly flat dust devil activity between roughly $L_s = 0°$ and 180°. The potential temperature gradient, which is related to the vigor of mixing, has a more pronounced peak in northern summer, but peaking just before $L_s = 150°$, a little later than the observed activity peak. Reconciling the observed activity peak with the peak in the TES thermodynamic data requires some process biasing activity to earlier seasonal dates. One possibility is to invoke the decrease in surface pressure occurring from $L_s = 60°$ to 150°. All else being equal, this will result in decreased near-surface air density and hence decreased sensible heat flux as the season progresses, potentially producing the necessary shift.

4.4. Why Amazonis?

[43] Amazonis is exceptional in our survey in terms of the number of active dust devils observed per unit area in both WA and NA images. It is therefore natural to ask whether one could predict this preeminence on the basis of a global assessment of the thermodynamic variables considered in section 4.3. Three key variables were the surface temperature and near-surface (~0–4 km) potential temperature gradient, which largely controls the sensible heat flux, and the PBL depth, which determines the thermodynamic efficiency. Maps of these variables for six periods during the annual cycle from the third MGS mapping year (the only complete year available without a global storm) are shown in Figures 9, 10, and 11, respectively. The location of the Amazonis seasonal study region on these maps is indicated with an asterisk.

[44] Figures 9, 10, and 11 confirm the seasonal trends at Amazonis of key thermodynamic variables shown in Figure 8, with values decreasing in northern autumn and winter. Globally, the effect of albedo on surface temperatures can most clearly be seen in northern spring and summer (dark regions are relatively warm, etc.), with the southern spring and summer temperatures peaking roughly in a zonal band near the subsolar latitude. The near-surface potential temperature gradient, which provides some information on the surface-air temperature contrast and hence the sensible heat flux, shows some similarity to the surface temperature plot, but with one major difference. While the latter shows highest values in southern summer, the former is biased to northern summer, suggesting that surface temperature increase from northern to southern summer is outstripped by the air temperature increase between these seasons. This is consistent with higher atmospheric dust opacities and hence higher direct solar heating of the atmosphere (and higher stability) in southern summer. In addition, the potential temperature gradient shows more

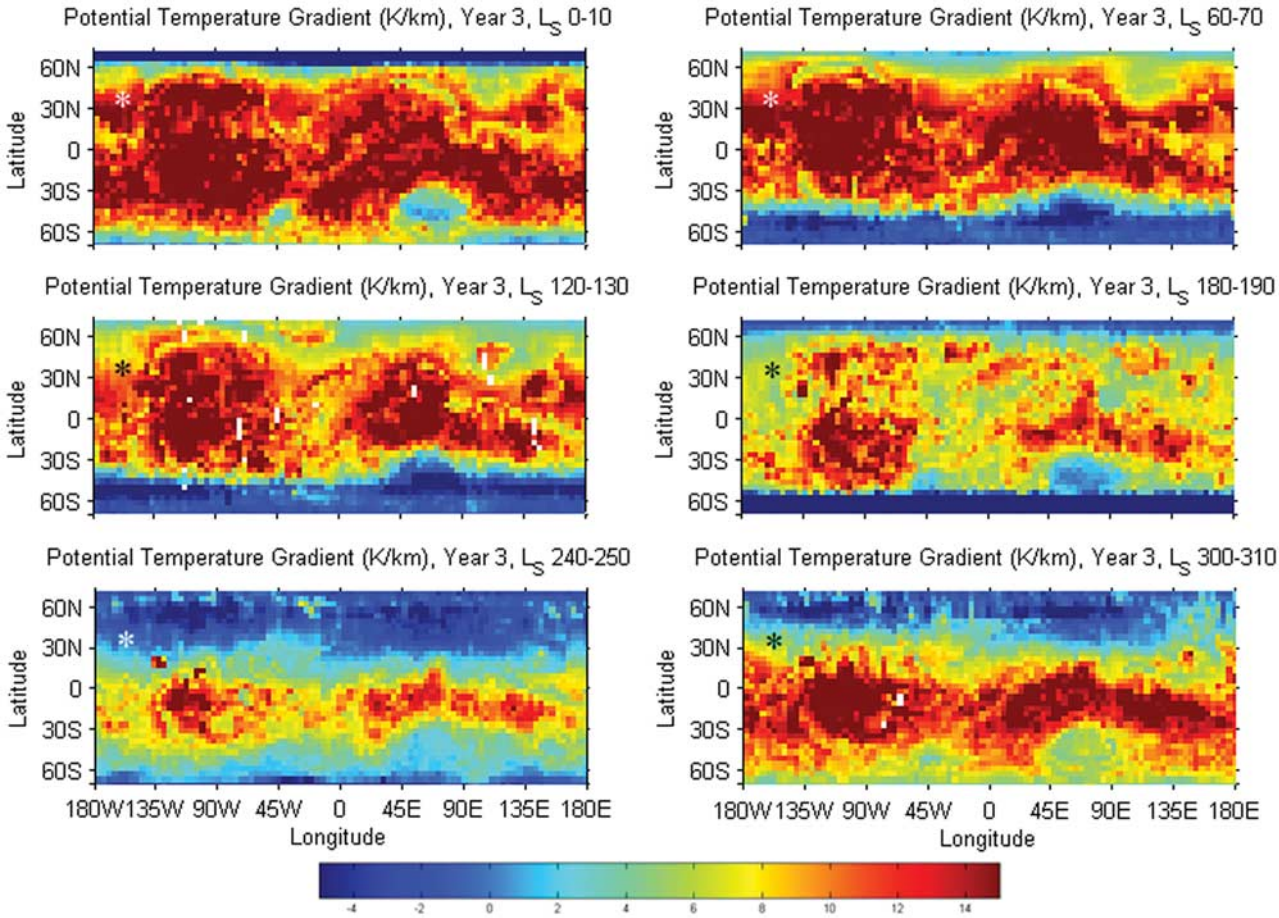

Figure 10. The geographical and seasonal distribution of the near surface potential temperature gradient (with positive values indicating a decrease of potential temperature with increasing height) estimated from TES retrieved surface temperature and 4.75 mbar temperature values. Color bar runs from −5 to 15 K/km.

geographical structure, for example, the relatively low gradient that traces the dichotomy boundary (Figures 10a–10c). While the surface temperature peak increases by about 20–30K between northern and southern summer, the peak maximum PBL height does not appreciably increase. The latitude range of deep PBL development and large potential temperature gradient is broadest near the equinoxes and narrowest at the solstices, with southern summer having the most restricted latitudinal range. This appears consistent with GCM predictions of dust devil activity in southern summer [*Newman et al.*, 2002; *Basu et al.*, 2004].

[45] While the figures show significant geographical structure in both fields, the figures do not provide a ''smoking-gun'' explanation for the unusually vigorous activity at Amazonis. For example, Cimmerium in southern spring and summer ought to have greater dust devil activity than Amazonis in the corresponding northern seasons, as it exhibits higher surface temperatures, deeper PBL development, and similar near-surface potential temperature gradient. As a result, the unusual activity in Amazonis may require a more detailed explanation involving the surface dust availability (maybe we just do not see the vortices in other places), and/or the mesoscale meteorology influenced by local-scale topography and other surface properties (maybe something suppresses the vortices in other places or enhances their activity at Amazonis).

5. Dust Devil Sizes

[46] Width and height measurements were made for a number of dust devils identified in the study. The widths and heights were measured from dust devil shadows using the solar incidence angle and assumption of a flat surface. The flat-surface assumption does not introduce significant error. Compared to the assumed flat surface, a slope of 5° yields an error in shadow-derived dust devil measurements of about 5%. Surfaces on scales greater than 35 km with slopes greater than 5° are rare on Mars (in an areal sense [*Aharonson et al.*, 2001]). Although slopes on smaller scales can be significantly larger, we specifically avoided examining shadows on topography that could be identified in the ~230 m/pixel images. For the NA images, the heights and widths were measured over three trials (i.e., each dust devil in each image was measured three separate times to minimize counting error) for all observed dust devils whose full shadows were visible in the images. Due to the small size of dust devils in the WA images, dust devil widths were not measured in these images, and heights were measured

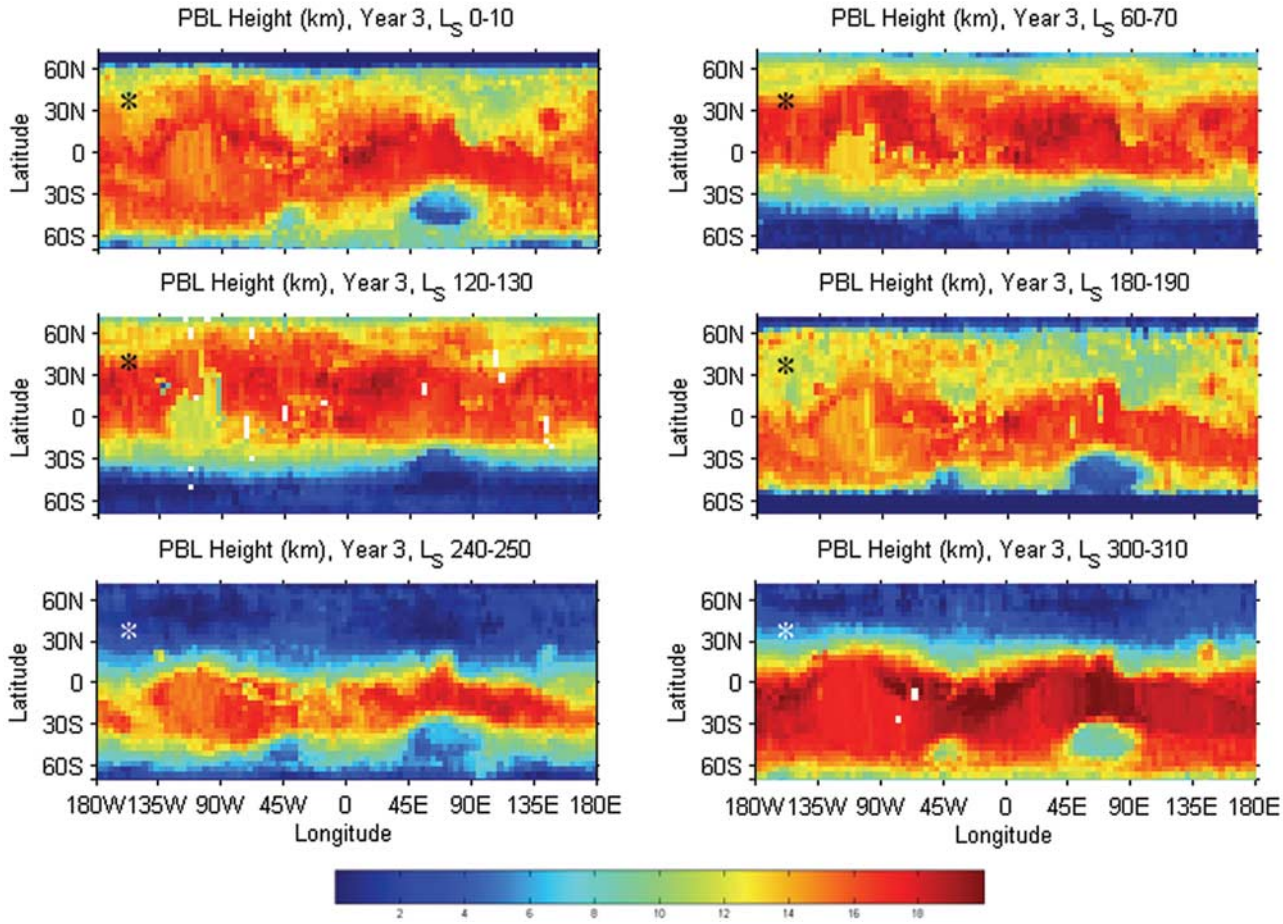

Figure 11. The geographical and seasonal distribution of maximum PBL top height estimated from TES data (see Figure 8 caption and the text). Color bar runs from 0 to 20 km.

only for the largest visible dust devils. Ten separate estimates of the dust devil heights were made for each dust devil measured in the WA images (i.e., they were remeasured on separate occasions), allowing an error estimate to be made.

[47] The resultant measurements are shown in Tables 5, 6, and 7. The tallest dust devil observed in our sample was an 8.5 km structure in Amazonis. The dust devils observed in the NA images ranged in height from 170 m to 1.8 km and in width from 28 m to 509 m. The measured dust devils in the WA images ranged in height from 3.8 to 8.5 km. Note that the NA dust devils are smaller than the WA dust devils for the population of images examined, but that this results from the lack of sampling of the largest dust devils in the NA images (the area covered by these images was sufficiently small that the lack of observation of a large dust devil is ascribable to chance; if one were sampled, it would easily have been visible in any of the NA images) and the insensitivity of the WA images to the smaller ones (they were not resolved by the WA camera).

6. Summary

[48] The MGS MOC WA and NA cameras have provided a powerful and unique opportunity to study dust devil activity on Mars. The number of available images is very large (>175,000), and consequently our initial survey of dust devils and dust devil tracks focused on nine regional study areas (Figure 2), selected on the basis of numerical model predictions, historical association with dust lifting, collocation with landed spacecraft, and our own initial browsing of the MOC database. This seasonally-resolved survey showed very large variations in the observed number of dust devils and dust devil tracks between the different regions, with in general no correlation between the number of images containing dust devils and the number containing tracks (Figure 3). The largest number of dust devils by far was observed in Amazonis (25–45°N, 145–165°W), while Casius (45–65° N, 255–285°W) exhibited the largest number of dust devil tracks. For both dust devils and dust devil tracks, local spring and summer were the preferred season of occurrence. The lack of observation of tracks at all sites during at least one season is taken to indicate that dust devil tracks are erased on a timescale of roughly a year or less.

[49] The observation of strong dust devil activity but relatively weak track development at Amazonis, contrasting with the extensive track formation at Casius in the absence of observed dust devils, prompts some interesting questions. Is ~2 pm (the time at which the images were collected) the best time to observe dust devils in all regions, and if not,

Table 5. Widths of Dust Devils Determined From NA MOC Images[a]

Image	Location	Average	Standard Deviation	Resolution, m	Width, m
m0300435	Amazonis	14.82	0.71	6.12	91
e0202175	Amazonis	7.40	0.47	12.34	91
e0202175	Amazonis	12.89	0.64	12.34	159
e0202175	Amazonis	5.28	0.39	12.34	65
e0202175	Amazonis	29.23	2.40	12.34	361
e0300938	Amazonis	5.22	0.31	6.14	32
e0300938	Amazonis	8.52	0.38	6.14	52
e0301651	Amazonis	27.02	0.49	9.22	249
e0301651	Amazonis	5.35	0.27	9.22	49
e0302304	Amazonis	37.29	1.47	12.3	459
e0302711	Amazonis	65.17	0.40	4.59	299
e0400765	Amazonis	8.21	0.55	9.25	76
e0400765	Amazonis	5.48	0.13	9.25	51
e0401708	Amazonis	4.82	0.25	9.28	45
e0401708	Amazonis	3.07	0.07	9.28	29
e0500695	Amazonis	2.63	0.28	12.34	32
e0501343	Amazonis	6.40	0.00	12.31	79
e0502077	Amazonis	3.35	0.37	12.28	41
e0502077	Amazonis	5.72	0.08	12.28	70
e0502077	Amazonis	10.95	0.33	12.28	134
e0502077	Amazonis	7.36	0.32	12.28	90
e0600037	Amazonis	41.52	0.85	12.27	509
m0202530	Sinus Meridiani	5.37	0.45	5.81	31
m0900193	Sinus Meridiani	41.14	0.49	2.88	118
m0300396	Chryse	8.37	0.44	5.96	50
m1300139	Chryse	38.17	1.34	8.83	337
m0301869	Sinai Planum	20.46	0.39	5.68	116
m0104498	Mare Cimmerium	11.70	0.26	11.31	132

[a]The widths refer to the subjective visible widths of the visible dust plumes. The column labeled ''Average'' is the average number of pixels counted across that dust devil.

why should this vary with location? How important are the details of the surface dust cover, for example, does a thicker dust layer make it easier to see visible dust devils but harder to produce tracks? That the curvilinear tracks (Figure 1) are not formed by dust devils is a problematic suggestion due to their rapid (subseasonal) formation and erasure timescales, and the need to invoke an as yet unknown additional formation process (linear wind streaks are easy to distinguish from dust devil tracks, for example).

[50] The abundance of dust devils in all regions except Amazonis was so low that few conclusions about seasonal trends could be drawn with any confidence. However, targeted imaging of a subset of Amazonis starting in the second MGS mapping year allowed quantitative analysis to

Table 6. Heights of Dust Devils Observed in NA MOC Images[a]

Image	Location	Average	Standard Deviation	Resolution	Incidence	Height, m
m0300435	Amazonis	46.23	1.85	6.12	44.65	286
e0202175	Amazonis	73.37	1.18	12.34	36.27	1234
e0202175	Amazonis	67.21	1.63	12.34	36.27	1130
e0202175	Amazonis	106.53	2.47	12.34	36.27	1792
e0301651	Amazonis	152.77	1.96	9.22	39.84	1688
e0302304	Amazonis	12.01	0.02	12.3	41.12	169
e0302304	Amazonis	102.57	1.47	12.3	41.12	1445
e0400765	Amazonis	32.21	0.14	9.25	43.59	313
e0400765	Amazonis	53.34	0.59	9.25	43.59	518
e0401708	Amazonis	74.95	0.51	9.28	45.38	686
e0500695	Amazonis	56.00	0.28	12.34	48.5	611
e0501343	Amazonis	39.03	0.46	12.31	49.76	407
e0502077	Amazonis	31.49	1.21	12.28	50.91	314
e0502077	Amazonis	79.61	0.37	12.28	50.91	794
e0502077	Amazonis	99.59	0.42	12.28	50.91	994
e0600037	Amazonis	38.93	0.91	12.27	52.98	360
m0202530	Sinus Meridiani	25.67	0.94	5.81	39.37	182
m1300139	Chryse	64.05	1.65	8.83	36.82	755
m0301869	Sinai Planum	69.17	1.79	5.68	42.9	423
m0104498	Mare Cimmerium	47.49	0.74	11.31	49.33	461

[a]The column labeled ''Average'' is the pixel count corresponding to the dust devil height measurement. The resolution of the image is given in meters.

Table 7. Heights of Dust Devils Observed in WA MOC Images[a]

Image	Location	Average	Standard Deviation	Resolution	Incidence	Height, m
m0101092	Amazonis	13.77	0.98	252.35	34.73	5012
m0101279	Amazonis	12.48	1.26	259.13	39.44	3932
m0101279	Amazonis	17.57	2.20	259.13	39.44	5536
m0101279	Amazonis	25.56	1.53	259.13	39.44	8051
m0101485	Amazonis	26.67	0.93	258.98	39.18	8473
m0101875	Amazonis	22.90	1.27	254.70	38.42	7353
m0102267	Amazonis	24.69	1.69	254.00	38.40	7911
m0102674	Amazonis	28.51	1.41	337.66	62.54	5002
m0103324	Amazonis	21.83	0.89	399.00	66.48	3791
m0103324	Amazonis	23.17	0.81	399.00	66.48	4024
m0201908	Amazonis	16.22	1.07	256.94	38.77	5190
e0300363	Amazonis	17.20	1.65	316.62	57.58	3460
e0301649	Amazonis	15.87	1.06	262.67	46.91	3900
e0600036	Amazonis	24.93	1.02	257.77	54.98	4502

[a]The column labeled "Average" is the pixel count corresponding to the dust devil height measurement. The resolution of the image is given in meters and the solar incidence angle in degrees.

be undertaken. This seasonal study site was centered on 36°N and 160°W, and a degree or so on a side (Figure 2). Dust devils were counted in each WA image, yielding the number per unit area as a function of season (Figure 5). A peak activity of just less than 2.5×10^{-3} km^{-2} was found, with no activity throughout essentially all of northern autumn and winter. The rise from zero in spring and the decline in late summer is smooth (there is no "cliff" or discontinuity in activity that can be seen), but with the decline more rapid than the rise. The third mapping year data show higher activity than the second, but this is more likely due to differential image quality than true interannual variability.

[51] If the peak number of dust devils per unit area is converted into a dust injection rate then Amazonis is roughly an order of magnitude more active than the Pathfinder landing site region (if the 2 pm activity at Amazonis is taken as representative). Taking the injection rate numbers to have an order of magnitude uncertainty, then the injection rates are sufficient to balance (or locally outstrip) deposition, supporting the idea that dust devils can supply the background haze of dust perennially observed in the atmosphere.

[52] Comparison of MOC and THEMIS images for the Amazonis seasonal study site during the third mapping year suggests that even at the peak of northern summer activity in the ~2 pm MOC images, the dust devil activity has terminated by the ~5 pm local time imaged by THEMIS (Table 4). This is consistent with late afternoon/evening collapse of boundary layer turbulence. Comparison of the MOC dust devil activity data with thermal data from TES suggests that the activity is strongly linked to the thermal drive for convection (compare Figures 5 and 8). The northern spring and summer peak in dust devil activity correlates well with high surface temperatures, large lower-atmosphere potential temperature gradients (indicating boundary layer instability and the drive for convection), and deepening of the planetary boundary layer. While locally there is a strong link between variables derived from the TES thermal data and the dust devil survey, when examined globally, the TES data do not yield an obvious explanation for the preeminence of Amazonis as a site for dust devil activity (Figures 9, 10, and 11). The role of the local scale atmospheric circulation in aiding or suppressing large dust devil formation, and that of tractability of the surface dust deposits for allowing convective vortices to become visible, need to be examined.

[53] Finally, the MOC WA and NA images allow the physical dimensions of dust devils large enough to be observed from orbit (Figure 7) to be estimated. From NA images, dust devils in the range of 30–500 m wide and 280 m to 1.8 km tall have been measured (Tables 5 and 6). From WA images, dust devils with heights estimated to be between 3.5 and 8.5 km have been observed (Table 7). These taller dust devils appear likely to extend through the full depth of the maximum daytime, well-mixed planetary boundary layer.

[54] **Acknowledgments.** We thank Lori Fenton and an anonymous reviewer for comments and suggestions that greatly improved this work. This project was supported in part by the Mars Data Analysis Program. Jenny Fisher took part in this research as a part of the Caltech Summer Undergraduate Research Fellowship Program.

References

Aharonson, O., M. T. Zuber, and D. H. Rothman (2001), Statistics of Mars' topography from the Mars Orbiter Laser Altimeter: Slopes, correlations, and physical models, *J. Geophys. Res.*, *106*(E10), 23,723–23,735.

Balme, M. R., P. L. Whelley, and R. Greeley (2003), Mars: Dust devil track survey in Argyre Planitia and Hellas Basin, *J. Geophys. Res.*, *108*(E8), 5086, doi:10.1029/2003JE002096.

Basu, S., M. I. Richardson, and R. J. Wilson (2004), Simulation of the Martian dust cycle with the GFDL Mars GCM, *J. Geophys. Res.*, *109*, E11006, doi:10.1029/2004JE002243.

Briggs, G. A., W. A. Baum, and J. Barnes (1979), Viking Orbiter imaging observations of dust in the Martian atmosphere, *J. Geophys. Res.*, *84*(B6), 2795–2820.

Cantor, B. A., P. B. James, M. Caplinger, and M. J. Wolff (2001), Martian dust storms: 1999 Mars Orbiter Camera observations, *J. Geophys. Res.*, *106*(E10), 23,653–23,687.

Cantor, B., M. Malin, and K. S. Edgett (2002), Multiyear Mars Orbiter Camera (MOC) observations of repeated Martian weather phenomena during the northern summer season, *J. Geophys. Res.*, *107*(E3), 5014, doi:10.1029/2001JE001588.

Christensen, P. R., et al. (2001), Mars Global Surveyor Thermal Emission Spectrometer experiment: Investigation description and surface science results, *J. Geophys. Res.*, *106*(E10), 23,823–23,871.

Colburn, D. S., J. B. Pollack, and R. M. Haberle (1989), Diurnal variations in optical depth at Mars, *Icarus*, *79*(1), 159–189.

Conrath, B. J., J. C. Pearl, M. D. Smith, W. C. Maguire, P. R. Christensen, S. Dason, and M. S. Kaelberer (2000), Mars Global Surveyor Thermal Emission Spectrometer (TES) observations: Atmospheric temperatures

during aerobraking and science phasing, *J. Geophys. Res.*, *105*(E4), 9509–9519.
Fenton, L. K., J. C. Pearl, and T. Z. Martin (1997), Mapping Mariner 9 dust opacities, *Icarus*, *130*(1), 115–124.
Ferri, F., P. H. Smith, M. Lemmon, and N. O. Rennó (2003), Dust devils as observed by Mars Pathfinder, *J. Geophys. Res.*, *108*(E12), 5133, doi:10.1029/2000JE001421.
Gierasch, P., and R. Goody (1967), An approximate calculation of radiative heating and radiative equilibrium in Martian atmosphere, *Planet. Space Sci.*, *15*(10), 1465–1477.
Grant, J. A., and P. H. Schultz (1987), Possible tornado-like tracks on Mars, *Science*, *237*(4817), 883–885.
Greeley, R., M. R. Balme, J. D. Iversen, S. Metzger, R. Mickelson, J. Phoreman, and B. White (2003), Martian dust devils: Laboratory simulations of particle threshold, *J. Geophys. Res.*, *108*(E5), 5041, doi:10.1029/2002JE001987.
Haberle, R. M., H. C. Houben, R. Hertenstein, and T. Herdtle (1993), A boundary-layer model for Mars: Comparison with Viking lander and entry data, *J. Atmos. Sci.*, *50*(11), 1544–1559.
Kahn, R. A., T. Z. Martin, R. W. Zurek, and S. W. Lee (1992), The Martian dust cycle, in *Mars*, edited by H. H. Kieffer et al., pp. 1017–1053, Univ. of Ariz. Press, Tucson.
Liu, J., M. I. Richardson, and R. J. Wilson (2003), An assessment of the global, seasonal, and interannual spacecraft record of Martian climate in the thermal infrared, *J. Geophys. Res.*, *108*(E8), 5089, doi:10.1029/2002JE001921.
Malin, M. C., and K. S. Edgett (2001), Mars Global Surveyor Mars Orbiter Camera: Interplanetary cruise through primary mission, *J. Geophys. Res.*, *106*(E10), 23,429–23,570.
Malin, M. C., G. E. Danielson, A. P. Ingersoll, H. Masursky, J. Veverka, M. A. Ravine, and T. A. Soulanille (1992), Mars Observer Camera, *J. Geophys. Res.*, *97*(E5), 7699–7718.
Martin, T. Z., and M. I. Richardson (1993), New dust opacity mapping from Viking Infrared Thermal Mapper data, *J. Geophys. Res.*, *98*(E6), 10,941–10,949.
Metzger, S. M., J. R. Carr, J. R. Johnson, T. J. Parker, and M. T. Lemmon (1999), Dust devil vortices seen by the Mars Pathfinder camera, *Geophys. Res. Lett.*, *26*(18), 2781–2784.
Murphy, J. R., and S. Nelli (2002), Mars Pathfinder convective vortices: Frequency of occurrence, *Geophys. Res. Lett.*, *29*(23), 2103, doi:10.1029/2002GL015214.
Newman, C. E., S. R. Lewis, P. L. Read, and F. Forget (2002), Modeling the Martian dust cycle: 1. Representations of dust transport processes, *J. Geophys. Res.*, *107*(E12), 5123, doi:10.1029/2002JE001910.
Renno, N. O., M. L. Burkett, and M. P. Larkin (1998), A simple thermodynamical theory for dust devils, *J. Atmos. Sci.*, *55*(21), 3244–3252.
Schofield, J. T., J. R. Barnes, D. Crisp, R. M. Haberle, S. Larsen, J. A. Magalhaes, J. R. Murphy, A. Seiff, and G. Wilson (1997), The Mars Pathfinder atmospheric structure investigation meteorology (ASI/MET) experiment, *Science*, *278*(5344), 1752–1758.
Smith, M. D. (2004), Interannual variability in TES atmospheric observations of Mars during 1999–2003, *Icarus*, *167*(1), 148–165.
Smith, M. D., B. J. Conrath, J. C. Pearl, and P. R. Christensen (2002), Thermal Emission Spectrometer observations of Martian planet-encircling dust storm 2001A, *Icarus*, *157*(1), 259–263.
Squyres, S. W., et al. (2003), Athena Mars rover science investigation, *J. Geophys. Res.*, *108*(E12), 8062, doi:10.1029/2003JE002121.
Strausberg, M. J., H. Wang, M. I. Richardson, S. P. Ewald, and A. D. Toigo (2005), Observations of the initiation and evolution of the 2001 Mars global dust storm, *J. Geophys. Res*, doi:10.1029/2004JE002361, in press.
Thomas, P., and P. J. Gierasch (1985), Dust devils on Mars, *Science*, *230*(4722), 175–177.
Toigo, A. D., and M. I. Richardson (2000), Seasonal variation of aerosols in the Martian atmosphere, *J. Geophys. Res.*, *105*(E2), 4109–4121.
Toigo, A. D., M. I. Richardson, S. P. Ewald, and P. J. Gierasch (2003), Numerical simulation of Martian dust devils, *J. Geophys. Res.*, *108*(E6), 5047, doi:10.1029/2002JE002002.
Zurek, R. W., J. R. Barnes, R. M. Haberle, J. B. Pollack, J. E. Tilman, and C. B. Leovy (1992), Dynamics of the atmosphere of Mars, in *Mars*, edited by H. H. Kieffer et al., pp. 835–933, Univ. of Ariz. Press, Tucson.

S. Basu, S. P. Ewald, J. A. Fisher, C. E. Newman, M. I. Richardson, and M. A. Szwast, Division of Geological and Planetary Sciences, California Institute of Technology, MS 150-21, Pasadena, CA 91125, USA. (mir@gps.caltech.edu)

C. Graf, La Canada High School, La Canada, CA 91011, USA.

A. D. Toigo, Department of Earth and Planetary Systems Science, Kobe University, Kobe, Japan.

R. J. Wilson, Geophysical Fluid Dynamics Laboratory, Princeton, NJ, USA.